Available online at www.sciencedirect.com

jmr&t Journal of Materials Research and Technology

www.jmrt.com.br

Original Article

Microstructure and mechanical properties of laser welded Ti–10V–2Fe–3Al (Ti1023) titanium alloy

Ahmad Chamanfar[a,*], Meng-Fu Huang[b], Timotius Pasang[c], Masahiro Tsukamoto[d], Wojciech Z. Misiolek[a,b]

[a] Loewy Institute and Department of Materials Science and Engineering, Lehigh University, Bethlehem, PA 18015, USA
[b] Loewy Institute and Department of Mechanical Engineering and Mechanics, Lehigh University, Bethlehem, PA 18015, USA
[c] Department of Mechanical Engineering, Auckland University of Technology, Auckland 1010, New Zealand
[d] Joining and Welding Research Institute, Osaka University, Osaka 5670047, Japan

ARTICLE INFO

Article history:
Received 24 June 2019
Accepted 8 April 2020

Keywords:
Titanium alloy
Laser welding
Microstructure
Mechanical properties

ABSTRACT

The microstructure, microhardness, tensile properties, and fracture characteristics of the laser welded Ti–10V–2Fe–3Al (Ti1023) titanium alloy in the as-welded condition were examined. The mechanical properties were related to the microstructure development across the weld. In the base material (BM), the primary α phase with spherical and lath morphologies was dispersed in the β matrix. The volume fraction of the α phase in the heat affected zone (HAZ) decreased to some extent compared to the BM as a result of its partial dissolution and/or transformation to the β phase. In the fusion zone (FZ), primary α phase was completely transformed to the β phase. The BM exhibited a higher hardness than HAZ and FZ due to a higher volume fraction of the primary α phase, which is harder than β phase. The yield strength (YS) and ultimate tensile strength (UTS) of the weldments were somewhat lower than those of the BM due to the presence of a softer phase in the FZ and a lower volume fraction of the α phase in the HAZ. Also, the presence of porosity, undercut, concavity, and coarse columnar β grains in the FZ contributed to lower YS, UTS, and total elongation in the weldments in comparison to the unwelded material. Examination of the fracture surface in the weldment tensile samples indicated a mixed brittle and ductile fracture mode.

1. Introduction

Titanium alloys have been widely used in the aerospace industries as replacements for aluminum alloys and steel because of their attractive properties including high strength-to-weight ratio, high fatigue resistance, good stiffness and toughness, and excellent corrosion resistance at room and elevated temperatures [1–3]. In particular, β titanium alloys like Ti1023 have been widely used as different aerospace components such as landing gears, duct materials, sheet metal components, fasteners, and engine exhaust nozzles [4]. In titanium alloys, the molybdenum equivalent (Mo_{eq}) is expressed based on the wt.% of alloying elements as $Mo_{eq} = 1.00\ Mo + 0.28\ Nb + 0.22\ Ta + 0.40\ W + 0.67\ V + 1.25\ Cr + 1.25\ Ni + 1.70\ Mn + 1.70\ Co + 2.50$

* Corresponding author.
E-mail: ahmad.chamanfar@mail.mcgill.ca (A. Chamanfar).
https://doi.org/10.1016/j.jmrt.2020.04.028

Fe [5]. This parameter shows the β phase stability and is used as a guidance in design and processing of different alloys [6]. Bania [5] showed that if the Mo_{eq} for titanium alloys is higher than 10 wt.%, which is the case for Ti1023, β stabilizing elements (such as V, Fe, Mo, Co, Ta, Cr, Nb, Mn, W, and Ni) suppress the α′ martensite formation and thus, the β phase is preserved upon quenching from high temperatures. The microstructure of Ti1023 is typically composed of α phase dispersed in the β matrix [7]. The α and β have hexagonal close packed (HCP) and body centered cubic (BCC) crystal structures, respectively [8]. The α phase is harder than the β phase [8]. The size, morphology, and volume fraction of these phases can be controlled to attain the required mechanical properties for commercial applications. The β-transus temperature in Ti1023 is about 800 °C and the alloy is used at high temperatures up to 315 °C [2].

Welding is an important manufacturing and repair process for titanium alloys in the aerospace industry [9,10]. During welding process, the molten titanium alloys rapidly reacts with the atmosphere, especially with oxygen, hydrogen, and nitrogen, leading to weld metal embrittlement. To resolve this problem, welding must be done under protective gas environment or vacuum. Among different welding methods, laser beam welding is widely used for welding of titanium alloys because it has a high energy density and a low heat input leading to narrow FZ and HAZ, low distortion and residual stresses, and deep penetration [3,11–13]. It also allows a high welding speed and automation easiness due to precision, productivity, and repeatability compared with conventional arc welding methods [11,14]. Some works have been reported on microstructure and mechanical properties of laser welded titanium alloys. In particular, numerous studies on laser welding of dissimilar Ti alloys (*e.g.,* Ti–15 V–3 Cr–3 Al–3 Sn to Ti–6 Al–4 V (Ti64) [15]), Ti to Ni alloys (*e.g.,* Ti64 to Inconel-718 [16]) and Ti to stainless steel (*e.g.,* Ti64 to 304 SS [17]) and less on the welding of the similar or dissimilar β Ti alloys like Ti1023 have been conducted and reported in literature. Also, substantial studies on the mechanical properties and microstructure of similar laser welded commercially pure (CP) Ti [14,18] and Ti64 [19] which are respectively α and α + β Ti alloys have been carried out. These two latter alloys have a different response to the laser welding compared to the β alloys such as Ti1023.

As representative examples, Denney et al. [20] observed acicular α phase in the β grains in the HAZ and FZ of laser welded Ti64. In this process, the material is exposed to high temperatures leading to primary α phase transformation to β phase. Then, upon cooling cycle of the weld to room temperature, acicular α phase precipitated in the β grains. Also, Akman et al. [21] pointed out that the β grain size increased in the HAZ and FZ in Ti64 with increasing the laser power, as expected. Chamanfar et al. [8] reported that in laser welded Ti–6Al–2Sn–4Zr–2Mo (Ti6242), an α + β alloy, the hardness of the FZ was higher than that of the BM due to acicular α′ martensite formation in the FZ. In addition to studies on α + β titanium alloy weldments, some limited research on characteristics of welded β alloys (*e.g.,* Ti–5Al–5V–5Mo–3Cr (Ti5553)) has been also reported. Pasang et al. [22], indicated that in the laser welded Ti5553, the FZ was entirely composed of the β phase with a coarse and columnar dendritic morphology and a lower hardness than that of the BM. From tensile properties perspective, one of the major challenges for different grades of laser welded Ti alloys is the low ductility and brittle fracture due to the microstructure and defect formation in the FZ [23–25].

However, the microstructure and mechanical properties of laser welded Ti1023 have not been reported in the literature. Therefore, this study has been performed to evaluate the weldability of the Ti1023 alloy and alterations in the microstructure and mechanical properties across the weld. In addition, the fracture mechanisms of the weldments were investigated.

2. Experimental procedure

A Ti1023 block with 140 mm × 58 mm × 46 mm (length × width × thickness) dimensions were received from the North American Alloys (Westlake Village, CA, USA). The chemical composition of the Ti1023 alloy is presented in Table 1 according to the materials data sheet provided by the company. The Ti1023 block was sliced into 1.6 mm thick sheets by wire electro-discharge machining and then prepared for laser welding. The welding surfaces were cleaned with ethanol in order to remove any contaminations. The laser welding was performed at the Joining and Welding Research Institute at Osaka University. A continuous wave fiber laser on a TruDisk 16002 machine (Trumpf, Ditzingen, Germany), Fig. 1a, was used for the butt welding of 1.6 mm thick Ti1023 sheets. Welding was performed at a power of 1.2 kW and a constant welding speed of 150 cm/min. Beam diameter at the focus spot was 0.28 mm and the focal point was situated 2 mm below the top surface of the sheets to obtain an adequate power density. The laser beam was transferred through an optical fiber with a diameter of 0.2 mm and it was focused using a lens with a diameter of 280 mm. In all cases, the length of the weldments was about 100 mm to allow enough sampling.

The welding set up and the fixtures used in the experimental work are shown in Fig. 1b and c. The samples were placed in a box coupled with an argon gas shielding system to protect the weld from environment by creating an inert atmosphere. The protective argon gas with a high purity was purged in the box at a flow rate of 35 L/min for 30 s prior to welding. The gas was left running at the same flow rate during welding and at least for 20 s after completion of each weld to ensure a full protection from the atmosphere. In this manner, the contamination of the molten metal by oxygen, hydrogen, and nitrogen

Table 1 – Chemical composition of the Ti1023 alloy in wt.%.

Material	V	Fe	Al	O	H	C	N	Ti
Ti1023	10.22	1.85	3.08	<0.11	<0.015	<0.05	<0.05	Bal.

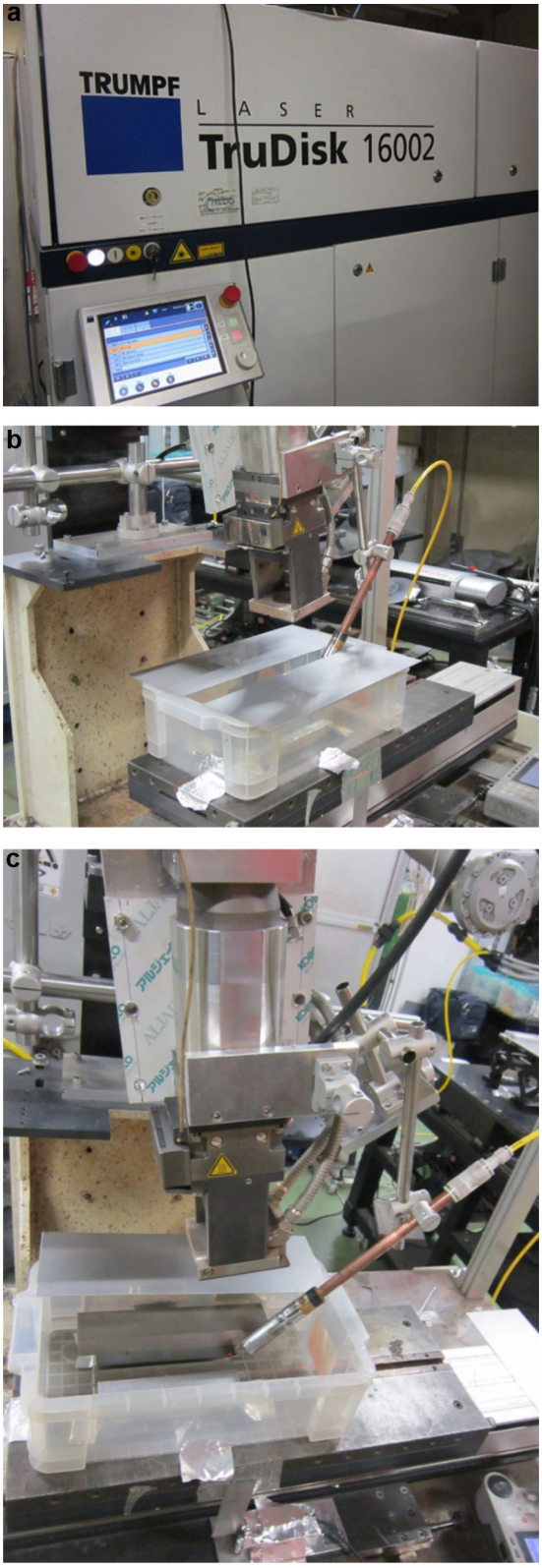

Fig. 1 – (a) The laser welding machine used in this study and (b and c) weld protection by argon gas flow in a box.

Table 2 – The laser welding process parameters used in this study.

Parameter	Value
Laser power, kW	1.2
Focal point position, mm	−2
Beam spot size (diameter), mm	0.28
Laser beam traveling speed, cm/min	150
Argon gas flow rate, L/min	35

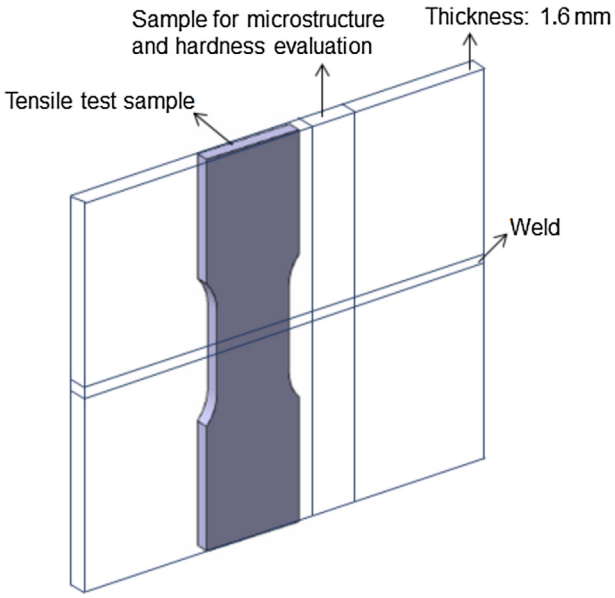

Fig. 2 – Location and orientation of the metallurgical characterization and tensile test samples with respect to the weld.

from the environment was minimized. The investigated laser welding process parameters are summarized in Table 2.

Numerous preliminarily weld trials performed under welding parameters outside of the current ranges were associated with metallurgical imperfections such as wide weld bead, intense underfill, lack of fusion, oxidation, gas inclusion, and excessive molten metal at the weld root, based on the visual inspections. Therefore, the reported parameters in Table 2 are based on many experiments that would allow reducing substantially the weld defects. Several representative weldments under these best welding conditions have been produced and analyzed. The aim of the current study was to examine the weldability of Ti1023 alloy especially microstructure, mechanical properties, and fracture characteristics of the weldments.

For microstructure analysis, the samples were cut perpendicular to the weld line (Fig. 2) and prepared using standard procedures including grinding by 320, 400 and 600 SiC grit paper and polishing with 6, 3, 1, and 0.25 μm diamond solutions. The sample surface was cleaned and dried after each grinding and polishing step. In addition, in order to reveal the microstructure of each zone, the sample surface was etched with Kroll's reagent consisted of 100 ml water, 6 ml HNO_3, and

3 ml HF. The light optical microscope and scanning electron microscope (SEM) were used in this study. The Olympus BH-2 optical microscope with Pax-it imaging camera and software were used to obtain the representative images. These images not only provided the morphology of both α and β phases but also allowed determination of the volume fraction and size of the primary α phase. The point counting method (ASTM E 562-02 standard) was used to determine the volume fractions of the α phase. For both volume fraction and size measurements, at least five micrographs were examined in each zone of the sample. For size measurements, at least 10 primary α phases were selected on each image. This gives a total of fifty size measurements for each zone of interest. For the secondary electron (SE) SEM and back-scattered electron (BSE) imaging, the Hitachi 4300SE was used for microstructure observations at higher magnifications.

Hardness across the weld (Fig. 2) was measured by an automated Leco® Microhardness Tester LM248AT with a 300 g load, 10 s dwell time, and a Vickers diamond pyramid indenter. The microhardness profiles were determined across the weld along three independent lines, which were 300 μm apart. At least twenty indents were measured on each line. Moreover, the distance between the indents on each line was 200 μm, about five times the indent diameter.

Three subsize ASTM E8 flat dog-bone samples with a gage length of 25 mm and a gage width of 6 mm were prepared from the welded sheets for tensile testing at an initial strain rate of $3 \times 10^{-3}\ s^{-1}$. The direction of the tensile samples was vertical with respect to the weld line (Fig. 2). A 30 kN Instron 5567 machine equipped with a digital image correlation system was used for tensile testing at room temperature. The latter was capable to record the distribution of elongation during tensile testing. The individual and average tensile properties are reported. Similar sample geometry and tensile testing approach was used for the as-received material for comparing the tensile properties of the weldments with those of the unwelded Ti1023 alloy. The fracture surface of the tensile samples was also examined with SEM.

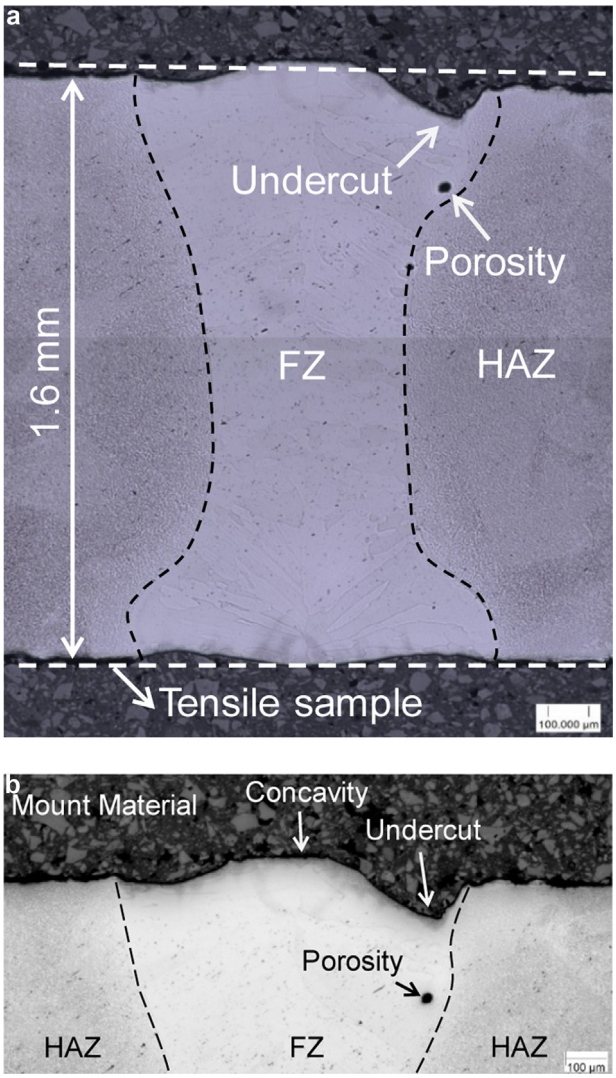

Fig. 3 – (a and b) Optical images presenting the appearance of the weld and the existence of undercut, concavity, and porosity in the FZ. The cross section in (a) shows the thickness (1.6 mm) of the sheet and the configuration of the tensile sample regarding the weld.

3. Results and discussion

3.1. *Weld appearance*

In Fig. 3 optical micrographs for the transverse cross-section of the weld are displayed. The sample was etched before optical microscopy examination to observe the geometrical characteristics of the weld. Under the investigated conditions a successful weld can be observed as supported by a proper seam geometry, full weld penetration, and complete fusion of the edges of the weld parts without excessive melting. A dog-bone or I-shaped FZ can be observed. In other words, the FZ is somewhat wider at the top and bottom and exhibited a narrower throat at the middle. This is related to non-uniform heat dissipation or cooling rates as the heat loss through the metal by conduction is faster than that near the surface by convection.

In terms of macroscopic defects, the FZ and HAZ appear to be crack free. In general, Ti alloys are less prone to solidification cracking in the FZ and liquation induced cracking in the HAZ than other alloys due to nonexistence of second phase particles and impurities [3,26,27]. As well, due to shielding with inert argon gas before, during, and after welding, the weld surface is free from oxidation.

However, an undercut can be observed on the side of the weld seam. As well concavity also exists at top and bottom of the weld. Undercut and concavity adversely affect the appearance of the weld bead and reduce the tensile properties, as discussed in Section 3.4. Undercut is a material loss imperfection generated by the evaporation of the melt during laser welding. Porosity with a spherical morphology was also detected in the FZ (Fig. 3a and b). Porosity is a frequent defect observed in fusion welding of titanium alloys including laser welding [2,3,28]. It has been observed in the laser welded CP Ti [3,29], Ti5553 [30], and Ti6242 [8]. It is generally attributed to the gas bubbles absorbed in the molten pool which cannot be released during solidification. For instance, surface

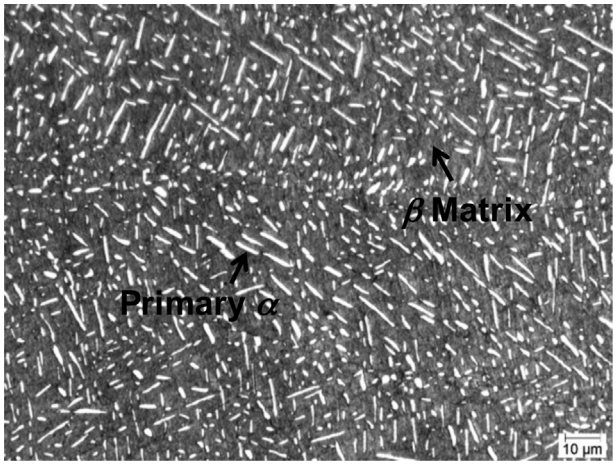

Fig. 4 – Light optical micrograph of Ti1023 BM showing the primary α (bright area) with bimodal distribution and β matrix (gray area).

contaminations of the workpiece by grease or oil can produce hydrogen bubbles during welding. Porosity usually reduces the strength of the weld, as discussed in Section 3.4.

3.2. *Microstructure across the weld*

The microstructure evolution during laser welding of Ti1023 alloy affects the mechanical properties and service capability. The light optical micrograph of the BM is shown in Fig. 4. The figure reveals the bimodal (spherical and lath) distribution of primary α phase (bright phase) dispersed in the β matrix (gray phase). In the BM Ti1023, the volume fraction and average size of the α phase were determined to be 40.1 ± 3.0% and 5.3 ± 4.0 μm, respectively. This result shows that there is a wide size distribution of the primary α phase in the BM. In particular, due to a bimodal (spherical and lath) morphology of primary α phase, the variation in the α phase size is considerable. Thus, size distribution was divided into two categories based on their morphologies. The sizes of the spherical and lath primary α phases were determined to be 1.6 ± 0.9 μm and 9.0 ± 1.8 μm, respectively. The presence of the spherical primary α phase provides ductility for the alloy [2].

During the laser welding process, the heat from the laser beam exposes the material to temperatures considerably higher than the β-transus temperature and melts the joint interface. Then, the material solidifies and a FZ is created. Also, the heat dissipates into the welding parts and creates a HAZ. As the laser moves away, the temperature rapidly decreases in the FZ and HAZ. Therefore, the microstructures of the BM, HAZ, and FZ are anticipated to be different from each other.

The optical microscopy images show that the weldment microstructure is strongly affected by the thermal cycle and cooling rate experienced during the laser welding. Fig. 5a reveals that in the HAZ the spherical and lath α phase are distributed in the β matrix. During laser welding, temperature increases in HAZ and partial dissolution and/or transformation of α phase to β phase occurs leading to a variation in the volume fraction and size of the α phase. This can be

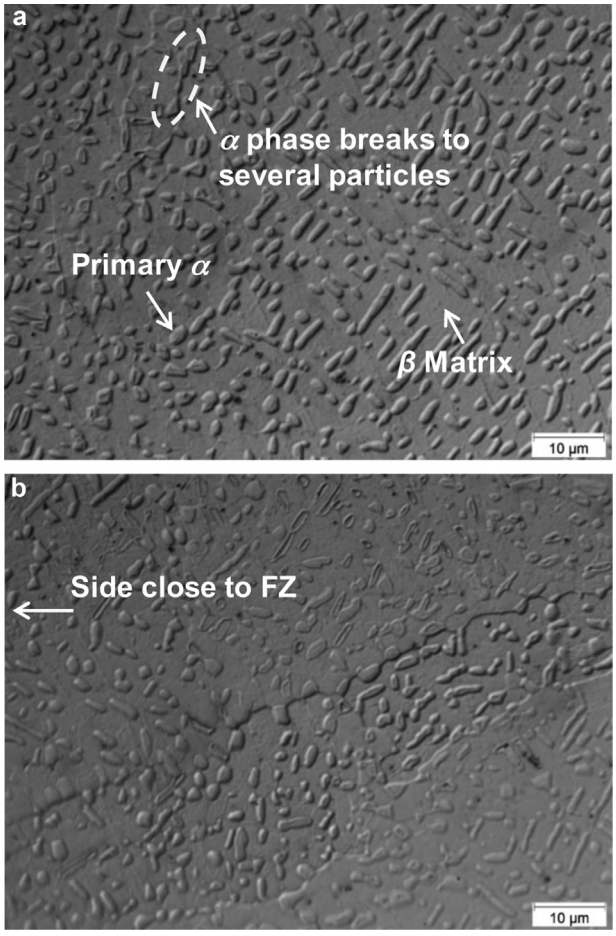

Fig. 5 – (a and b) Micrographs of the HAZ in the as-laser welded Ti1023 showing spherical and lath primary α phase distributed in the β matrix. In (b) the area close to the FZ is shown.

observed by comparing the volume fraction of the primary α phase in the HAZ (37.4 ± 3.0%) to that in the BM (40.1 ± 3.0%). In addition, the average size of the primary α phase was determined to be 3.5 ± 2.8 μm in HAZ which is smaller than that (5.3 ± 4.0 μm) in the BM. Moreover, in the HAZ, the sizes of the spherical and lath primary α phases were measured as 1.4 ± 0.4 μm and 5.5 ± 2.6 μm, respectively. They are smaller than those of the BM, *i.e.*, 1.6 ± 0.9 μm and 9.0 ± 1.8 μm, respectively.

The optical microstructure of HAZ close to the FZ is shown in Fig. 5b. In this area the material experiences a peak temperature higher the β-transus temperature (800 °C) during laser welding due to the proximity to the FZ, compared to areas close to BM where the peak temperature is lower than the β-transus. Therefore, it can be indicated that α phase is partially dissolved, broken up, and transformed to β phase, Fig. 5b. The complete transformation of α to β does not occur because of fast heating rate in the laser welding. The occurrence of these partial microstructure alterations can be also proved by comparing the volume fraction and size of the primary α phase in the HAZ and BM as shown in Fig. 6. The primary α phase volume fraction in the BM is higher than that in the HAZ to

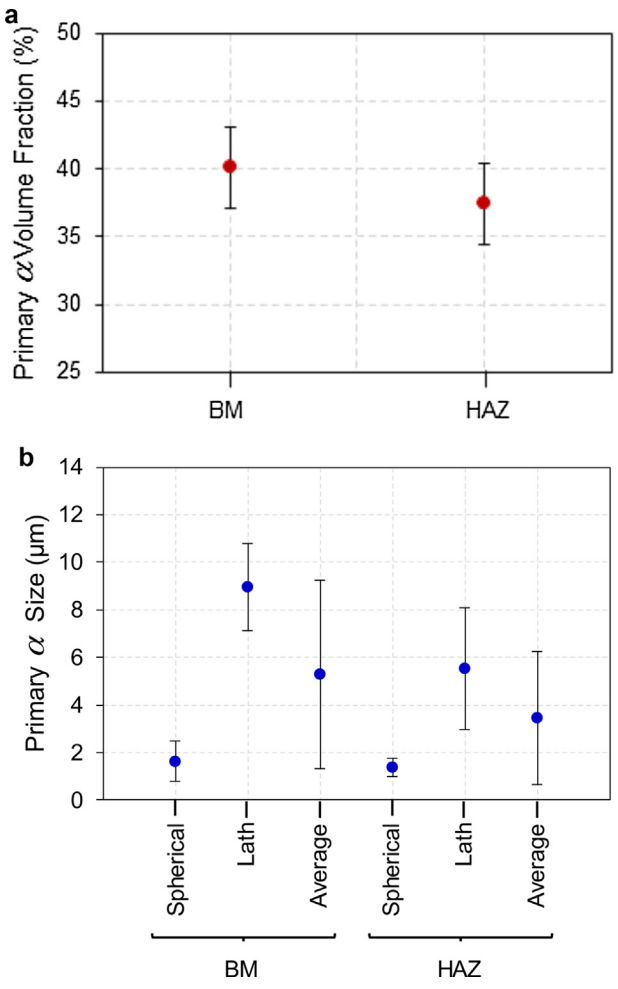

Fig. 6 – The primary α phase (a) volume fraction and (b) size within the BM and HAZ. The error bars represent the standard deviations in the measurements.

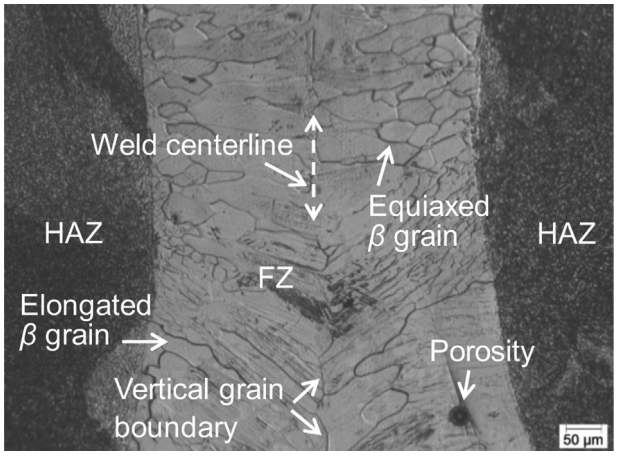

Fig. 7 – A light optical micrograph showing the FZ and HAZ microstructures in the as-laser welded Ti1023. The coarse columnar as well as equiaxed β grains and porosity can be seen in the FZ.

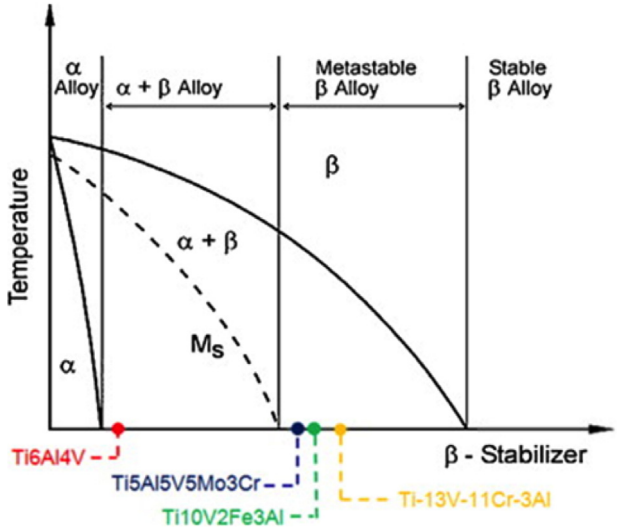

Fig. 8 – A phase diagram for several titanium alloys [32].

some extent. Furthermore, the average size of the primary α phase and its standard deviation within the BM are larger than those within the HAZ. This can be attributed to breaking up and partial dissolution of the lath particles in the HAZ (Fig. 5).

The size and shape of the grains in FZ depend on the heat flow during weld pool solidification [2]. As can be observed from Fig. 7 besides β phase, no α phase was present in the FZ. The β phase morphology in the FZ can be also seen in Fig. 7. The β grains in the FZ are coarse and have columnar (elongated) as well as equiaxed morphologies. The columnar grains can be formed due to preferential growth of grains along the opposite direction of the heat extraction during solidification, which is also known as epitaxial growth [3,14,31]. This columnar grain geometry was observed in the FZ of the electron beam welded Ti5553 as well [30]. Because of temperature gradients during laser welding from input energy, the temperature was the highest at the weld centerline and decreased toward both sides of the BM. Therefore, once laser source is moved away, β grains solidified from both side of the FZ adjacent to HAZ, toward the weld centerline and generated a grain boundary morphology vertical to the weld centerline (Fig. 7) [2].

During heating cycle of the weld, α to β transformation takes place in the FZ where temperature rapidly exceeds the β-transus temperature. This is supported by the phase diagram presented in Fig. 8 [32]. It can be observed that Ti1023 alloy locates outside of the start line (M_s) for diffusion less transformation of the β phase to the α′ martensite. Therefore, upon cooling β phase to the α′ martensite transformation as well as the β to α phase transformation are suppressed in the FZ due to the fast cooling rate of the laser welding process and presence of β-stabilizing elements such as V and Fe leading to a $[Mo]_{eq}$ greater than 10 wt.%. According to Mo_{eq} formula, the Mo_{eq} value for Ti1023 alloy is 11.45 wt.%. Also, the diffusivity of the β stabilizing elements is slow [2]. Thus, the transformed single β phase is retained in the FZ during cooling to the room temperature without any α′ martensite or α phase formation. Similarly, Bania [5] reported that in the metastable β titanium alloys, β phase is retained even at high cooling rates.

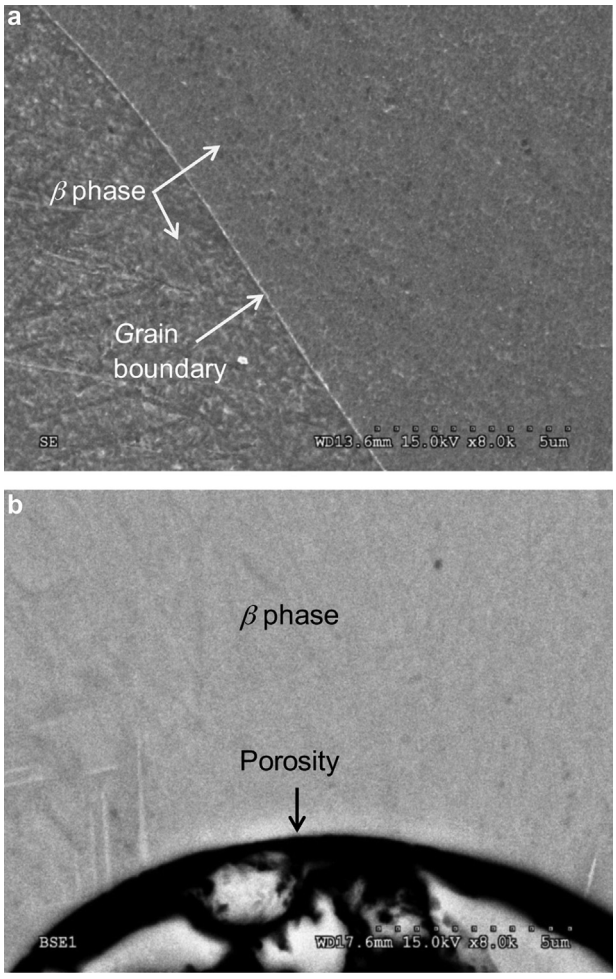

Fig. 9 – (a) SE-SEM image of the FZ showing the β phase and a β grain boundary and (b) BSE-SEM image of the FZ illustrating the β phase and porosity.

Consistently, Chen et al. [23] simulated the cooling rate during laser welding of Ti–22Al–25Nb (Ti2225) alloy as ~960 °C/s, which is substantially greater than the critical cooling rate of 120 °C/s for β transformation to other phases. In other words, for this investigated Ti2225 alloy, the single β phase can be preserved when the alloy is quenched from a temperature greater than the β-transus provided that the cooling rate is higher than 120 °C/s.

The presence of β phase in the FZ can be also observed and proved by the comparison of the SE-SEM (Fig. 9a) and BSE-SEM (Fig. 9b) images. Like the optical microscopy image (Fig. 7), the higher magnification SE-SEM image (Fig. 9a) still only shows the β phase and its grain boundary. To observe the BSE-SEM image (Fig. 9b), the characteristics of the β phase and features of the BSE imaging have been combined and applied. In titanium alloys, the β phase forms because of the presence of β phase stabilizing elements such as V and Fe [32]. In the BSE imaging, atomic number or chemical compositional contrast can be used for phase identification [33]. In a flat and even metallographically polished surface, the back-scattered electrons are in certain relationship to the atomic number: regions of low atomic number will be darker than the regions of high atomic number. In Ti1023 alloy, the α phase stabilizer is Al, and the β phase stabilizers are V and Fe. Also, the atomic number of these elements are 13, 23, and 26, respectively. Therefore, the area containing high amount of Al should be dark and the area containing high amount of V and Fe should be bright. In the BSE image (Fig. 9b) there is no dark area except for the porosity. In other words, this entire bright BSE image shows that only β phase is present in the FZ.

3.3. *Microhardness across the weld*

The microhardness profiles across the weld in the as-welded condition are plotted in Fig. 10. The profiles were measured near the top surface, at the middle, and near the bottom surface of the sample. It can be observed that the three measured microhardness profiles are relatively close to each other. BM hardness (378 ± 7 HV) is higher than the hardness values of the HAZ (320 ± 14 HV) and FZ (327 ± 5 HV). The crystal structure of α phase is HCP and that of the β phase is BCC. Thus, it can be expected that α phase is harder than β phase as there are less slip systems for dislocation movement in the HCP crystal structure of the α phase than BCC in the β phase. In other words, for the Ti1023 alloy the precipitation of the α phase in the β matrix is the main hardening mechanism. According to the quantitative microstructural data (Fig. 6), α phase volume fraction in the BM is higher than that of the HAZ. Therefore, the BM is harder than the HAZ in the as-weld Ti1023. Also, the BM hardness is higher than that of the FZ since in the FZ only the β phase was present (Figs. 7 and 9). In addition, based on the microhardness profile, laser welding creates quite narrow FZ (600 μm wide) and HAZ (1200 μm wide, together on both sides), due to the highly concentrated nature of the heat source and low heat input in this welding process.

3.4. *Tensile properties*

The configuration of the tensile sample with respect to the weld is represented in Fig. 3a. Also, Fig. 3a shows that the tensile sample contains the FZ, HAZ, and BM. The tensile properties of as-welded Ti1023 alloy are presented in Table 3. In order to compare the effect of laser-welding on the tensile properties, the corresponding properties of the unwelded (as-received) material are also provided in Table 3. The YS, UTS, and total elongation of the as-laser welded samples were 850 MPa, 945 MPa, and 2.1%, respectively. This means the YS, UTS, and total elongation are respectively 82%, 84%, and 24% of the BM values. In other words, the YS and UTS are comparable to those of the BM values while ductility is considerably lower. Other researchers [25,31,34] have also observed a significant decrease in the tensile ductility in laser welded Ti alloys compared to the unwelded material. For instance, Wang et al. [31] reported a total elongation of 1.9% in laser welded Ti–24Al–15Nb which is significantly lower than the value (12.8%) for the as-received alloy.

In addition, by investigating the strain map of the tensile test sample (Fig. 11; where different colors specify different strain levels), the FZ + HAZ exhibited higher strains compared to the BM. This agrees with a lower hardness in the FZ and HAZ regions compared with the BM. Moreover, the fracture location in the tensile samples was within the FZ.

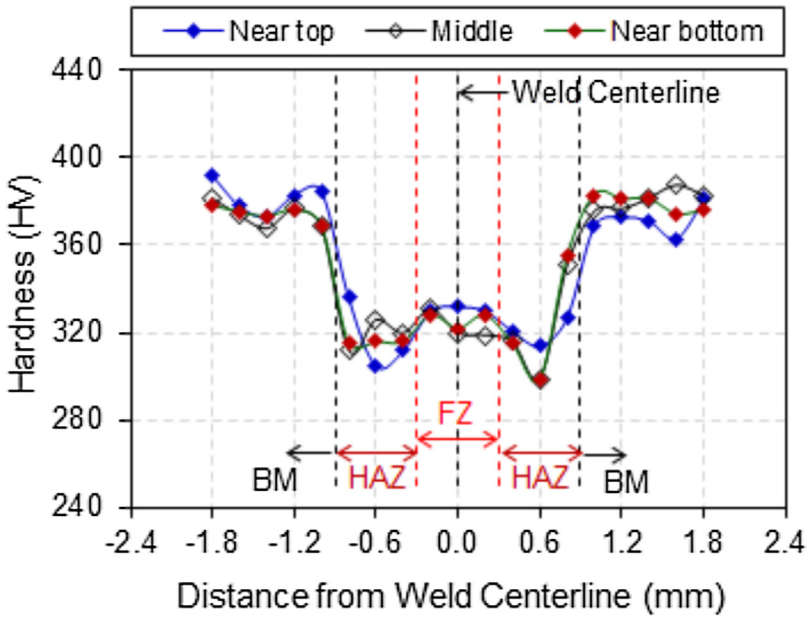

Fig. 10 – Microhardness profile across the weld in the as-laser welded Ti1023.

Table 3 – Tensile properties of the as-laser welded and unwelded (as-received) Ti1023. The individual tensile properties for each tensile test are presented in the parenthesis in front of the average corresponding properties.

Conditions	YS (MPa)	UTS (MPa)	Total elongation (%)
As-laser welded	850 ± 18 (830, 855, 865)	945 ± 13 (930, 950, 955)	2.1 ± 0.3 (1.8, 2.2, 2.4)
As-received	1032 ± 10 (1020, 1035, 1040)	1128 ± 30 (1100, 1125, 1160)	8.7 ± 1.5 (10, 7, 9)

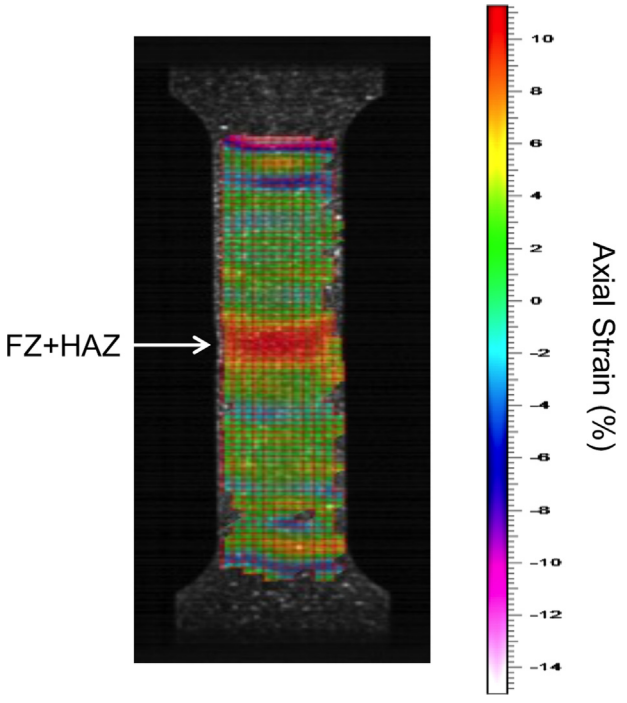

Fig. 11 – Strain map of the sample during tensile testing. The different colors specify different strain levels.

The lower tensile properties in the weldment can be attributed to microstructure changes as well as the presence of porosity, undercut, concavity, and tensile residual stresses. The gage length of the tensile sample from the weldment is consisted of FZ, HAZ, and BM with different microstructures (Figs. 4–7). This contrasts with the gage length of the tensile sample from the as-received material where a single microstructure exists. Therefore, the results of the tensile test are expected to be different for the weldment from the as-received material. The microstructure changes across the weld resulted in a lower hardness values in the FZ and HAZ compared to the BM. Therefore, it is expected that the YS and UTS for weldment are lower than those of the unwelded material. Consistently, Boyer et al. [35] indicated that the UTS decreases in titanium alloys as the hardness decreases. Also, porosity (Fig. 3) and the undercut at the edge of the FZ could act as the local stress concentration sites. Similarly, stress concentration occurs at the edges of concavity. As geometrical discontinuities, porosity and undercut also decrease the effective cross-sectional area of the FZ and thus, decrease the load bearing capability. This all results in reduced YS, UTS, and total elongation values. Moreover, it is pointed out [36] that the presence of residual tensile stresses in the laser welded Ti alloys reduces the effective YS and UTS compared with the unwelded material.

In addition, the coarse and columnar solidification structure in the FZ (Fig. 7), is not capable to sustain the plastic

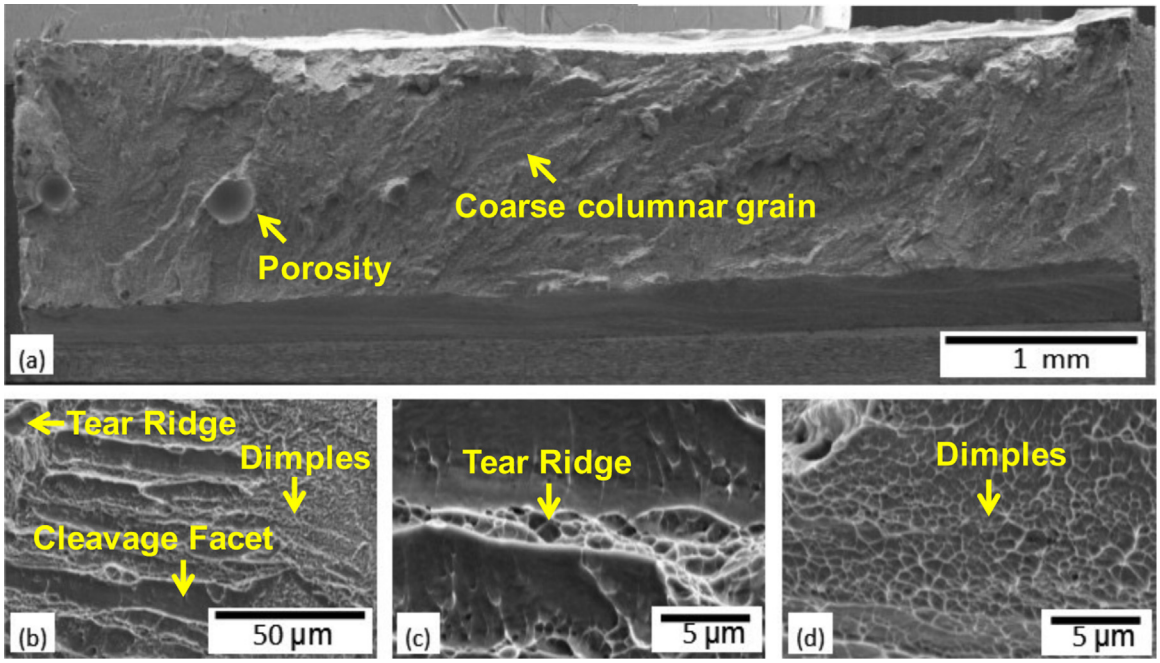

Fig. 12 – SEM images showing the fracture surface of an as-welded tensile sample. (a) Overall fracture surface and (b–d) higher magnification images demonstrating a mixed brittle (cleavage facets) and ductile (dimples and tear ridges) fracture mode.

deformation during tensile loading to the unwelded material extent. This results in a lower tensile ductility. Consistently, *in situ* tensile testing has proved [24] that grain boundaries of the coarse and columnar grains in the FZ of laser welded Ti alloys are stress concentration and thus cracking nucleation sites during tensile loading. The coarse and columnar grains in the FZ are reported [24] to be the primary factor in low ductility of Ti laser welds due to easier crack initiation and propagation along these boundaries. This issue is even more severe when the orientation of the columnar grains is vertical to the tensile loading direction [37]. In summary, the grain morphology in the FZ reduces considerably the ductility of the weldment as well.

3.5. *Fractography*

In all as-welded tensile samples fractured occurred in the FZ because of its lower hardness (strength) than HAZ and BM as well as presence of porosity, undercut, concavity, and coarse columnar grains in the FZ. Fig. 12a shows the overall fracture surface containing porosity. Porosity decreases the effective cross-sectional area of the weld for sustaining the tensile load and is most likely the initiation site of the failure and triggers fracture in the FZ. In addition, existence of coarse columnar grains illustrates probable intergranular microcrack initiation, propagation, and fracture as another fracture mechanism. In Fig. 12b a higher magnification image is presented which proves a mixed brittle and ductile fracture. The brittle fracture is evidenced by intergranular cleavage facets (separation) and the ductile fracture is verified by presence of transgranular dimples and tear ridges. Considerable number of dimples on the fracture surface implies that the tensile sample has undergone plastic deformation before fracture, and it is a sign of ductile fracture. In Fig. 12c cleavage facets with prior-β grain boundaries and dimples on the grain boundaries are visible at a higher magnification. Crack propagation along the longitudinal direction of the columnar grains creates the cleavage facets. The solidification structure of the FZ generated a partially brittle structure. And finally, in Fig. 12d shallow dimples can be observed which indicates some degree of ductility. In summary, the fracture mode is identified as a mixed brittle and ductile fracture mode, based on the observed fracture patterns. The fracture mode agrees with the limited ductility of the weld.

4. Conclusions

The Ti–10V–2Fe–3Al (Ti1023) alloy was effectively laser welded. The quality of the as-laser welded alloy was evaluated by investigating the microstructure, existence of metallurgical defects, microhardness, tensile properties, and fracture mechanisms. The following conclusions can be drawn from this study:

1. The spherical and lath α phase was observed in the β matrix in the base material (BM). In the heat affected zone (HAZ), the thermal cycle of the welding process led to partial transformation of α to β and decreased the average size and content of the α phase to some extent.
2. The microstructure in the fusion zone (FZ) of this β alloy was entirely consisted of β grains with coarse columnar as well as equiaxed morphologies. The formation of α′ martensite or α phase was suppressed because of the fast cooling rate in the laser welding process and the high

amount of β stabilizing alloying elements such as V and Fe.

3. The hardness measurements indicated a higher hardness in the BM compared to the HAZ and FZ due to a higher volume fraction of the α phase in the BM, which is harder than the β matrix.
4. The yield strength (YS), ultimate tensile strength (UTS), and total elongation of the weldments were 82%, 84%, and 24% of the values for the unwelded alloy, respectively. The presence of porosity, undercut, concavity and coarse columnar β grains in the FZ as well as a lower α content in the HAZ reduced the tensile properties in the weldments.
5. During tensile testing fracture occurred in the FZ for all samples because of the microstructural features of the FZ and an overall lower hardness. The existence of intergranular cleavage facets on the fracture surface was a sign of brittle fracture whereas presence of transgranular dimples and tear ridges demonstrated a ductile fracture. Thus, a mixed brittle and ductile fracture mode was operative.

Conflicts of interest

None declared.

Acknowledgements

The authors would like to thank the Loewy Family Foundation for financial support of this study as well as the partial financial support for the authors, AC as Loewy Postdoctoral Fellow, TP as Loewy Visiting Professor, and WZM as Loewy Professor through the Loewy Institute endowment at Lehigh University. As well, the authors are thankful to Mr. Masami Mizutami from the Joining and Welding Research Institute at Osaka University in Japan for conducting the laser welding experiments.

REFERENCES

[1] Titanium alloy guide. RMI Titanium Company; 2000. p. 1–5.
[2] Donachie MJ. Titanium, a technical guide. 2nd ed. ASM International; 2000.
[3] Palanivel R, Dinaharan I, Laubscher RF. Microstructure evolution and mechanical characterization of Nd:YAG laser beam welded titanium tubes. Mater Charact 2017;134:225–35.
[4] Boyer RR. An overview on the use of titanium in the aerospace industry. Mater Sci Eng A 1996;213:103–14.
[5] Bania PJ. Beta titanium alloys in the 1990s. In: Eylon D, Boyer RR, Koss DA, editors. Beta titanium alloys in the 1990s. Warrendale, PA: TMS; 1993. p. 3–14.
[6] Zhou T, Aindow M, Alpay SP, Blackburn MJ, Wu MH. Pseudo-elastic deformation behavior in a Ti/Mo-based alloy. Scr Mater 2004;50:343–8.
[7] Lei L, Huang X, Wang M, Wang L, Qin J, Li H, et al. Effect of hot compressive deformation on the martensite transformation of Ti–10V–2Fe–3Al titanium alloy. Mater Sci Eng A 2011;530:591–601.
[8] Chamanfar A, Pasang T, Ventura A, Misiolek WZ. Mechanical properties and microstructure of laser welded Ti–6Al–2Sn–4Zr–2Mo (Ti6242) titanium alloy. Mater Sci Eng A 2016;663:213–24.
[9] Nakai M, Niinomi M, Akahori T, Hayashi K, Itsumi Y, Murakami S, et al. Microstructural factors determining mechanical properties of laser-welded Ti–4.5Al–2.5Cr–1.2Fe–0.1C alloy for use in next-generation aircraft. Mater Sci Eng A 2012;550:55–65.
[10] Junaid M, Nawaz Khan F, Bakhsh N, Nadeem Baig M, Rahman K. Study of microstructure, mechanical properties and residual stresses in full penetration electron beam welded Ti–5Al–2.5Sn alloy sheet. Mater Des 2018;139:198–211.
[11] Fang X, Liu H, Zhang J. Reducing the underfill rate of pulsed laser welding of titanium alloy through the application of a transversal pre-extrusion load. J Mater Proc Technol 2015;220:124–34.
[12] Liu J, Watanabe I, Yoshida K, Atsuta M. Joint strength of laser-welded titanium. Dent Mater 2002;18(2):143–8.
[13] Yunlian Q, Ju D, Quan H, Liying Z. Electron beam welding, laser beam welding and gas tungsten arc welding of titanium sheet. Mater Sci Eng A 2000;280:177–81.
[14] Maawad E, Gan W, Hofmann M, Ventzke V, Riekehr S, Brokmeier H-G, et al. Influence of crystallographic texture on the microstructure, tensile properties and residual stress state of laser-welded titanium joints. Mater Des 2016;101:137–45.
[15] Hsieh CT, Shiue RK, Huang R-T, Tsay LW. The effect of post-weld heat treatment on the microstructure and notched tensile fracture of Ti–15V–3Cr–3Al–3Sn toTi–6Al–4V dissimilar laser welds. Mater Sci Eng A 2016;653:139–46.
[16] Liu J, Liu H, Gao X-L, Yu H. Microstructure and mechanical properties of laser welding of Ti6Al4V to Inconel 718 using Nb/Cu interlayer. J Mater Proc Technol 2020;277:116467.
[17] Elmi Hosseini SR, Feng K, Nie P, Zhang K, Huang J, Li Z, et al. Enhanced strength of 304 SS–Ti6Al4V laser-welded joints containing composite interlayers. J Mater Eng Perform 2018;27:6135–48.
[18] Li C, Muneharua K, Takao S, Kouji H. Fiber laser–GMA hybrid welding of commercially pure titanium. Mater Des 2009;30:109–14.
[19] Kumar C, Das M, Paul CP, Bindra KS. Weld quality assessment in fiber laser weldments of Ti–6Al–4V alloy. J Mater Eng Perform 2019;28(5):3048–62.
[20] Denney PE, Metzbower EA. Laser beam welding of titanium. Weld Res Suppl 1989:342–8.
[21] Akman E, Demir A, Canel T, Sinmazcelik T. Laser welding of Ti6Al4V titanium alloys. J Mater Process Technol 2009;209:3705–13.
[22] Pasang T, Sánchez Amaya JM, Tao Y, Amaya-Vazquez MR, Botana FJ, Sabol JC, et al. Comparison of Ti–5Al–5V–5Mo–3Cr welds performed by laser beam, electron beam and gas tungsten arc welding. Proc Eng 2013;63:397–404.
[23] Chen Y, Zhang K, Hu X, Lei Z, Ni L. Study on laser welding of a Ti–22Al–25Nb alloy: microstructural evolution and high temperature brittle behavior. J Alloys Compd 2016;681:175–85.
[24] He B, Tian X-J, Cheng X, Li J, Wang H-M. Effect of weld repair on microstructure and mechanical properties of laser additive manufactured Ti-55511 alloy. Mater Des 2017;119:437–45.
[25] Lei Z, Zhou H, Chen Y, Zhang K, Li B. A comparative study of deformation behaviors between laser-welded joints and base metal of Ti–22Al–24.5Nb–0.5Mo alloy. J Mater Eng Perform 2019;28:5009–20.
[26] Chamanfar A, Jahazi M, Gholipour J, Wanjara P, Yue S. Suppressed liquation and microcracking in linear friction welded Waspaloy. Mater Des 2012;36:113–22.
[27] Chamanfar A, Valberg HS, Templin B, Plumeri JE, Misiolek MZ. Development and validation of a finite-element model for isothermal forging of a nickel-base superalloy. Materialia 2019;6:100319.
[28] Fang X, Zhang J. Effects of microstructure and concavity on damage behavior of laser beam welded Ti–2Al–1.5Mn

titanium alloy joints. Int J Adv Manuf Technol 2015;79:1557–68.
[29] Torkamany MJ, Malek Ghaini F, Papan E, Dadras S. Process optimization in titanium welding with pulsed Nd:YAG laser. Sci Adv Mater 2012;4:489–96.
[30] Sabol JC, Pasang T, Misiolek WZ, Williams JC. Localized tensile strain distribution and metallurgy of electron beam welded Ti–5Al–5V–5Mo–3Cr titanium alloys. J Mater Process Technol 2012;212:2380–5.
[31] Wang L, Sun D, Li H, Shen C. Effects of postweld heat treatment on microstructure and properties of laser-welded Ti–24Al–15Nb alloy joint. J Mater Eng Perform 2019;28(11):6827–35.
[32] Lutjering G, Williams JC. Titanium. 2nd ed. Springer-Verlag; 2003.
[33] Goldstein J, Newbury DE, Joy DC, Lyman CE, Echlin P, Lifshin E, et al. Scanning electron microscopy and X-ray microanalysis. 3rd ed. Kluwer Academic/Plenum Publishers; 2003.
[34] Lei ZL, Dong ZJ, Chen YB, Huang L, Zhu RC. Microstructure and mechanical properties of laser welded Ti–22Al–27Nb/TC4 dissimilar alloys. Mater Sci Eng A 2013;559:909–16.
[35] Boyer R, Welsch G, Collings EW. Materials properties handbook: titanium alloys. ASM International; 1994.
[36] Junaid M, Baig MN, Shamir M, Khan FN, Rehman K, Haider J. A comparative study of pulsed laser and pulsed TIG welding of Ti–5Al–2.5Sn titanium alloy sheet. J Mater Process Technol 2017;242:24–38.
[37] Kong B, Liu G, Wang D, Wang K, Yuan S. Microstructural investigations for laser welded joints of Ti–22Al–25Nb alloy sheets upon large deformation at elevated temperature. Mater Des 2016;90:723–32.